

# Energy reliability enhancement of a data center/wind hybrid DC network using superconducting magnetic energy storage



Xiaoyuan Chen<sup>a</sup>, Mingshun Zhang<sup>a</sup>, Shan Jiang<sup>a</sup>, Huayu Gou<sup>a</sup>, Pang Zhou<sup>a</sup>, Ruohuan Yang<sup>b,\*</sup>, Boyang Shen<sup>c,d,\*\*</sup>

<sup>a</sup> School of Engineering, Sichuan Normal University, Chengdu, 610101, China

<sup>b</sup> School of Electrical Automation and Information Engineering, Tianjin University, Tianjin, 300072, China

<sup>c</sup> Department of Engineering, University of Cambridge, Cambridge, CB3 0FA, United Kingdom

<sup>d</sup> Clare Hall, University of Cambridge, Cambridge, CB3 9AL, United Kingdom

## ARTICLE INFO

### Keywords:

Superconducting magnetic energy storage (SMES)

Interline energy conversion

Medium-voltage direct-current (MVDC) distribution  
Doubly-fed induction generator (DFIG)

## ABSTRACT

The progressive penetrations of sensitive renewables and DC loads have presented a formidable challenge to the DC energy reliability. This paper proposes a new solution using series-connected interline superconducting magnetic energy storage (SCI-SMES) to implement the simultaneous transient energy management and load protection of DC doubly-fed induction generator (DC-DFIG)/internet data center (IDC) composites medium-voltage direct-current (MVDC) network. The SCI-SMES mainly consists of two current source converters (CSCs) sharing a common SMES link. It can implement the transient energy conversion and interaction between sensitive sources and loads in two individual DC feeders, even they are with different voltage and current levels. To prove the above-mentioned functions, a kW-class experimental SCI-SMES prototype is established. For actual renewable energy scenarios, six different cases of power flow and energy interaction between DC-DFIG and IDC are presented in this paper, and a MW-class with SCI-SMES-integrated hybrid DC network is built in simulation for verification. A techno-economic assessment, considering capital investment, operating cost, and financial losses of voltage sags, shows that the total investment payback period is in the range of 5.44–18.41 years, which proves the SCI-SMES has both economic and technical advantages in large-scale data centers and renewable generation sectors.

## 1. Introduction

Taken the advantages of concise power-grid structure and cost-effective operation, medium-voltage (MV) direct-current (DC) distribution systems have become increasingly popular, and has been regarded as one of the promising solutions to the establishment of 100% renewable energy system [1,2]. DC-characterized power system elements such as distributed generators (DGs) [3,4], energy storage devices (ESDs) [5, 6], electric vehicles (EVs) [7,8] and internet data centers (IDC) [9,10] can be integrated into the DC distribution systems saving additional converting stages. Unpredictable power intermittence of renewable sources can be directly smoothed by energy storages, without considerations of reactive power, frequency stability and phase angle issues in AC systems.

MV DC power system is expected to take a significant status in future

smart grid architecture, but DC fault ride-through (FRT) capability is a major challenge against the widespread adoption of MV DC power system [11,12]. In previous studies, common codes demanded island operations of the MV DC power systems in power quality cases of over currents and abnormal voltages, even very slight faults. However, considering that the penetration of the MV DC power system in AC utility power system is hopefully prevailing in the near future [13,14], many references have pointed that the MV DC power systems should continuously connect to the utility grid for a specified period (e.g., the demand of fault ride-through grid codes [15,16]), to support the transient voltage stability [17] or to avoid imbalanced power supply and consumption [18]. That is, electricity producers and consumers inside the MV DC power system should be equipped with FRT capability.

Unfortunately, crucial loads and generators represented by IDCs and DC doubly-fed induction generators (DC-DFIGs) are sensitive to power

\* Corresponding author.

\*\* Corresponding author.

E-mail addresses: [yrh9312@163.com](mailto:yrh9312@163.com) (R. Yang), [bs506@cam.ac.uk](mailto:bs506@cam.ac.uk) (B. Shen).

quality disturbances. As reported in Ref. [19], poor power quality can result in millions of economic losses annually in IDC. Meanwhile, disconnection of the wind turbines will significantly exacerbate the imbalance between demand and supply, risking a region outage [20,21]. The vulnerabilities of these two sensitive applications in DC power system can be classified into two aspects, i.e., external and internal factors, summarized as follows:

- **External factor:** According to the DC fault characteristics [22,23], when a fault occurs in the DC power system, the DC voltage will change extremely fast, and the fault current could be several times larger than the rated value, damaging the fragile converters and causing shutdown of the DC loads and generators [24,25].
- **Internal factor:** Due to the directly-connected topology, the abrupt voltage change will induce a large electro-motive force (EMF) in the rotor side of the DC-DFIG, which will destroy the rotor-side converter (RSC) and gearbox from the inside [26]. Meanwhile, the constant power feature [27,28] of the IDC makes it easy to experience the over currents internally under severe voltage disturbances, damaging to critical components such as computers and air-conditioning systems [29].

As an emerging custom power device, series-connected custom power device (SCPD) is an optional solution to improve the performances such as the voltage compensation, which have been widely studied in utility grids for protection of sensitive loads [30,31], fault overcurrent limitation [32,33], stability of grid-connected renewable energy [34,35], and so on. Among SCPDs, dynamic voltage restorer (DVR) is the most technically advanced solution for power and voltage sag/swell mitigation [36,37]. DVR works via injecting a specific voltage in series into the transmission line to compensate energy sag and swell and regulate the distorted voltage waveforms in power systems. In DC power systems, some DC-DVRs and DC-DVR-attributive devices have been proposed in the existing literature that can be utilized for voltage maintenance, such as [38–43]. However, these DC-DVRs exist one of the following drawbacks: 1) Due to the inherent topology defects of the DCPETs, some DC-DVRs have a unidirectional voltage compensation capability, which makes the voltage compensators unable to deal with the DC voltage swell [38]. 2) Due to the passive design, some DC-DVRs have a limited voltage compensation range, which makes the voltage compensators only suitable for moderate voltage disturbances [39]. 3) Due to the complex structure and operation of large-scale ESDs, some DC-DVRs have expensive costs, which confine their large-scale popularizations [40,41].

Moreover, since the DC-DVRs are generally operated during abnormal grid conditions, the utilization rate of the ESD inside the DC-DVR is always low [42]. To increase the utilization rate of DC-DVRs for indirectly reducing the capital cost, the concept of interline DVR (IDVR) is proposed in the literature, for AC [43,44] and DC power system applications [45]. The core idea of this topology is to protect sensitive loads (even with different current and voltage level), and the power of these DVRs are supplied with a common ESDs. Inspired by this view, If the energy can be replenished dynamically by some means, the DC-DVRs will be capable of mitigating sags/swells with long durations. The applications of DC-DVRs in protection of DC-DFIGs provide a tactfully solution. The power flow between the DVR and the DC-DFIG is converse to that of the sensitive load (IDC) under voltage sags and swells, respectively. Under voltage sags, due to the low residual system voltage, the generated power from DC-DFIG that cannot be sent to the grid is stored into the ESD of the DVR, and vice versa [46,47]. Following this thought, if a DC-IDVR can be used to simultaneously serve for a DC-DFIG and an IDC located in different distribution feeders, under voltage sags, the generated energy surplus of the DC-DFIG can be transferred from the DC-IDVR to the power vacancy of the IDC. This will tremendously reduce the capacity requirement of the ESD.

Another challenge is the selection of the ESD type. Most of the

voltage-type ESDs cannot timely respond to the DC fault [48,49]. Thanks to the development of superconductivity, bringing various custom solutions in generation, transmission, and distribution [50,51]. Current-type ESDs, typified by superconducting magnetic energy storage (SMES), has a very short time delay (millisecond level) during either charge or discharge process. The power output is instantaneously available, and the response time almost depends on the activations of power electronic elements. What is more, the SMES has the advantages of very high efficiency (>95%), long cycle life [>1e6 (time)], and high power density [>1e4 (W/kg)] [52].

In this paper, a series-connected interline SMES (SCI-SMES) is designed. It comprises two current source converters (CSCs) with a common SMES link, where each CSC is interfaced in series with different DC feeders. An application scenario of a DC-DFIG/IDC hybrid MV DC power system is established in simulation for performance validation of the proposed SCI-SMES. The proposed SCI-SMES has the ability of both voltage sag and swell compensation and can be used for the DC-DFIG and IDC with different voltage, current, and power levels. The rarer and more commendable characteristic of the proposed SCI-SMES is that, the actions of each converter for voltage compensation are individual and would not cause influence to the other load. Compared to the existing DC power and energy regulators [38–43], the proposed SCI-SMES has the exclusive ability of multiple load protection, and also has the advantages of a large compensation range, no transformer, and fewer controlled switches.

Overall, the contributions of this paper can be summarized as follows:

- 1) An innovative concept of DC-DFIG/IDC hybrid MV DC network is proposed regarding multiple low-carbon energy generation sectors, consumers, and regulators.
- 2) A new hybrid MV DC network is developed with the consideration of multi-energy (wind energy, electrical energy, and magnetic energy) conversion and management, along with the characteristics of sensitive load uninterrupted power supply and renewable energy fault ride through safeguard.
- 3) The voltage restoration is implemented between the DC-DFIG and the IDC under power and energy disturbances. A promising SCI-SMES is designed with the power network configuration, control strategy, working principle, and reliable parameter estimation.
- 4) An experiment of the SCI-SMES and the simulation of the hybrid MV DC power system are implemented in this paper. Energy interactions under six conditions are considered to verify the protection performance of the SCI-SMES and the economic analysis.

The rest of the paper is organized as follows. Section 2 introduces the proposed hybrid MV DC power system, from the perspectives of the overall scheme, DC-DFIG, IDC, SCI-SMES, and power flow among these three devices. Section 3 presents the principle of the proposed SCI-SMES. Section 4 shows the experimental results of the SCI-SMES under various kinds of voltage disturbances. Section 5 shows a case study of the hybrid MV DC power system, considering the short-term and long-term energy disturbances, to verify the feasibility of the proposed cooperative energy management and protection. Section 6 shows the economic analysis of the SCI-SMES and the economic loss of the IDC and DC-DFIG, giving the results of the payback period. Section 7 concludes the characteristics and technical advantages of the SCI-SMES in actual renewable energy scenarios.

## 2. System overview

### 2.1. Overview of the proposed MVDC system

**Fig. 1** shows a conceptual framework of the MV DC power system. It contains photovoltaic and wind plant (i.e., DC-DFIG) as renewable

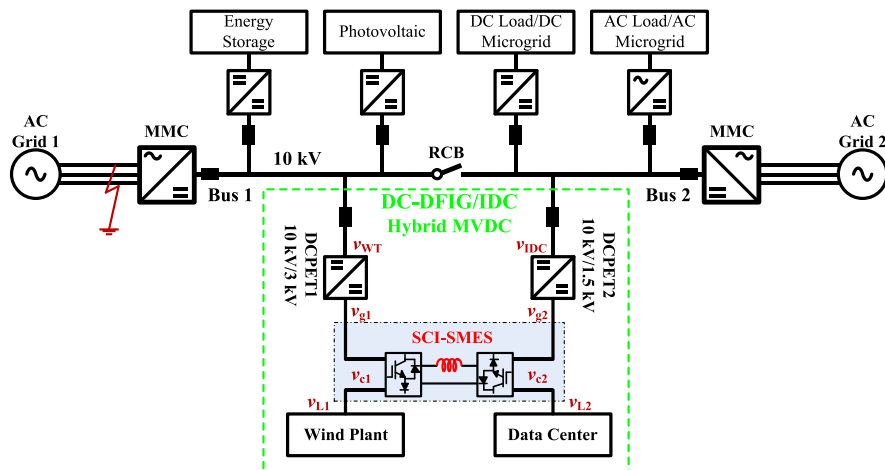


**Fig. 1.** Schematic diagram of the WT-IDC hybrid MVDC power system and the location of the proposed SCI-SMES device.

generators; DC load/DC microgrid, AC load/AC microgrid, and IDC as electricity consumer; and various kinds of energy storage as power flow regulator. The discussed MV DC power system is equipped with an RCB. When the RCB is ON, the Bus 1 and Bus 2 are allied with each other and the MV DC system is under unified operation. From Fig. 1, the hybrid MV DC power system is marked inside the green dotted box, which is the studied part in this paper, where  $v_{WT}$  and  $v_{IDC}$  represent the MV DC side voltage of the DC-DFIG and IDC;  $v_{g1}$  and  $v_{g2}$  represent the grid-side voltage after the transformation of the DCPET 1 and 2;  $v_{L1}$  and  $v_{L2}$  represent the terminal voltage of the DC-DFIG and IDC;  $v_{c1}$  and  $v_{c2}$  represent the compensated voltage from the SCI-SMES, respectively.

Fig. 2 shows the relationship of the multi-energy production, conversion, and transmission among DC-DFIG, IDC, SMES, and the two DCPETs (DCPET 1 and 2). The wind energy ( $P_1$ ) is captured by the DC-DFIG, and the produced electricity ( $P_2$ ) is transferred to the DCPET 1 ( $P_3$ ), flowing through the Converter 1 of the SCI-SMES. Meanwhile, the IDC is an electricity consumer, and the electric power is transferred from the DCPET 2 ( $P_6$ ) through the Converter 2 to the IDC ( $P_7$ ). The SCI-SMES is to maintain the two terminal voltages  $v_{L1}$  and  $v_{L2}$  at the rated values (i.e.,  $v_{L1}$  and  $v_{L2}$ ).

## 2.2. Power flow of SCI-SMES-integrated system

From Fig. 2, if the grid-side voltages are equal to the rated values of the DC-DFIG and IDC terminal voltages, the SCI-SMES has no power exchange with the transmission line, i.e.,  $P_4 = 0$  and  $P_5 = 0$ . To intuitively understand the energy conversion among the SCI-SMES and the transmission line of DC-DFIG and IDC, Fig. 3 gives the power flow under the above six kinds of voltage mismatching. When the grid-side voltages do not match the rated values of the two terminal voltages, the circumstances can be separately analyzed as follows:

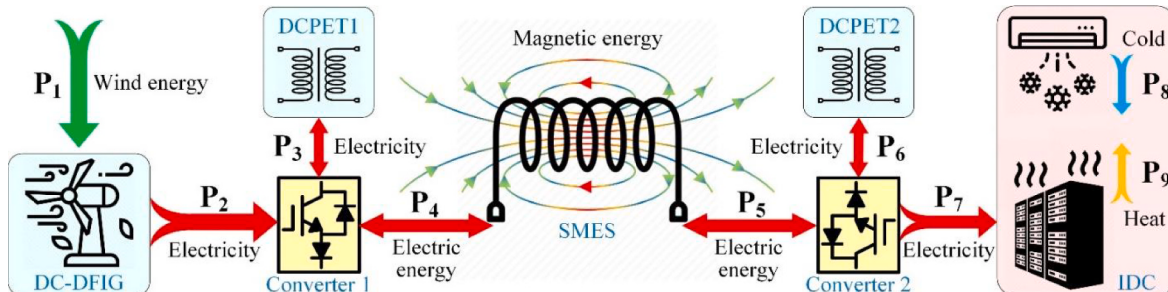


**Fig. 2.** Relationship of the multi-energy production, conversion, and management in the WT-IDC hybrid MVDC power system.

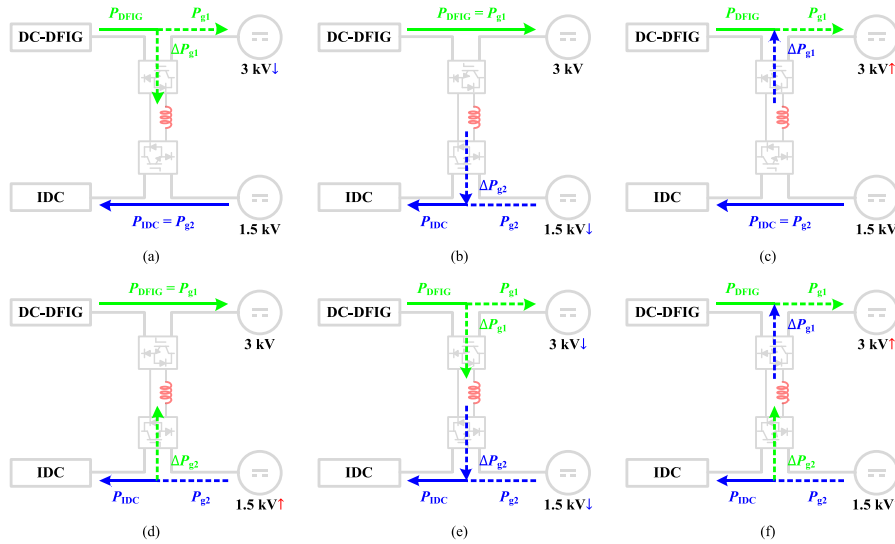


**Fig. 3.** Power flow and energy interaction among DC-DFIG, IDC, and SCI-SMES.

### 3. Modeling of DC-DFIG, IDC, and SCI-SMES

#### 3.1. DC-DFIG

Due to the board prospect of the MV DC power system, researchers have done lots of investigations to integrate the DFIG into the DC power system [53,54]. Many interface options have been proposed, and the application scenarios have been considered such as DC microgrids [55, 56], island power systems [57], and ship power generation [58]. Among the many DC-DFIG options, the topologies shown in Fig. 4 obtains the most attentions and have been widely studied. It is comprised of a wind turbine, a single-voltage-source-inverter (VSI), and an uncontrolled rectifier. It offers the advantage of inexpensive diode bridge and a derated-power VSI.

Momentum theory can be referred to analyze the behavior of the wind turbine. Assuming that the air is incompressible, and the studied variables are the same in a given section of the stream, Fig. 5 shows the process of capturing the wind energy based on disk-shaped actuator theory and Bernoulli's equation [65]. The input wind power can be expressed in the form of kinetic energy as:

$$P_w = \frac{1}{2} \rho A_1 V_w^3 \quad (1)$$

where  $\rho$  is the air density.  $V_w$  represents the input wind speed.

Whereas, the mechanical power  $P_{\text{mech}}$  captured by the wind turbine is relative with the power coefficient  $C_p(\lambda, \beta)$  and the radius of rotor blades  $R_{\text{mech}}$ . It can be expressed as:

$$P_{\text{mech}} = P_w - P'_w = \frac{1}{2} \rho \pi R_{\text{mech}}^2 V_w^3 C_p(\lambda, \beta) \quad (2)$$

The power coefficient  $C_p(\lambda, \beta)$  is a function of tip step ratio ( $\lambda$ ) and the

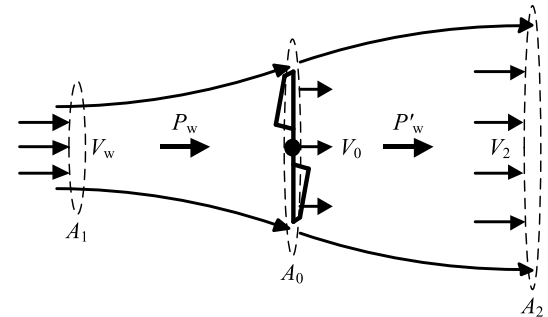


**Fig. 5.** Wind turbine aerodynamics based on disk-shaped actuator theory.

pitch angle ( $\beta$ ). Its empirical equation can be represented as follows [59]:

$$\left\{ \begin{array}{l} C_p(\lambda, \beta) = k_1 \left( \frac{k_2}{\lambda_i} - k_3 \beta - k_4 \beta^{k_5} - k_6 \right) e^{\frac{k_7}{\lambda_i}} \\ \lambda_i = \frac{1}{\lambda + k_8} \\ \lambda = \frac{R_{\text{mech}} \Omega_{\text{mech}}}{V_w} \end{array} \right. \quad (3)$$

where  $\Omega_{\text{mech}}$  is the rotor angular speed. For a specific wind turbine, coefficients  $k_1 \sim k_8$  are inherent.

According to the modeling of the DC-DFIG [34], the dynamic equation of the rotor voltage  $\vec{v}_r$  can be expressed as:

$$\vec{v}_r = \frac{L_m}{L_s} \frac{d\vec{\psi}_s}{dt} + \left( R_r + \sigma L_r \frac{d}{dt} \right) \vec{i}_r \quad (4)$$

where  $L_m$ ,  $L_s$ , and  $L_r$  represent the mutual, stator-side, and rotor-side inductance, respectively.  $\vec{\psi}_s$  represents the stator flux.  $\vec{i}_r$  represents the rotor current.  $\sigma$  represents the leakage coefficient;  $\sigma = 1 - L_m^2 / L_s L_r$ . In equation (4), the first component is the rotor electromotive force (EMF),  $\vec{e}_r$ , induced by the stator flux.

Due to the existence of the stator-side rectifier, the voltage will be clamped to a four step-shaped AC wave. If a voltage sag/swell occurs at  $t = 0$  with a voltage transformation ratio  $p$ , the stator voltage  $\vec{v}_s$  before and after the fault can be expressed as [53,54]:

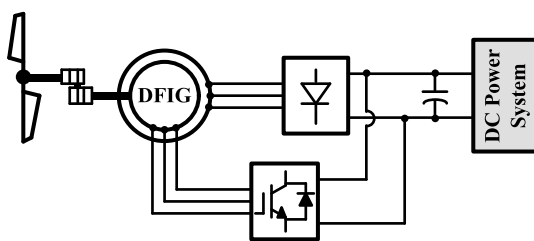


**Fig. 4.** Topology of DC-DFIG WECS interfaced to DC power system.

$$\vec{v}_s = \begin{cases} \frac{2V_{L1}}{\pi} \left[ e^{j\omega_s t} + \sum_{n=1}^{\infty} \frac{e^{\pm j(6n\pm 1)\omega_s t}}{6n \pm 1} \right] & t < 0 \\ \frac{2(1-p)V_{L1}}{\pi} \left[ e^{j\omega_s t} + \sum_{n=1}^{\infty} \frac{e^{\pm j(6n\pm 1)\omega_s t}}{6n \pm 1} \right] & t \geq 0 \end{cases} \quad (5)$$

where  $\omega_s$  represents the stator angular frequency. Neglecting the stator resistance, under normal operation, the rotor EMF can be expressed as:

$$\vec{e}_r^r = \frac{L_m}{L_s} \frac{d\vec{\psi}_s^r}{dt} = \frac{2V_{L1}}{\pi} \frac{L_m}{L_s} \left[ s e^{j\omega_{slip} t} + \sum_{n=1}^{\infty} \frac{6n \pm s}{(6n \pm 1)^2} e^{\pm j(6n\pm 1)\omega_s t} e^{-j\omega_r t} \right] \quad (6)$$

where  $s$  represents the slip.  $\omega_{slip}$  represents the slip angular frequency. Superscript  $r$  represents that the expression is in the rotor frame. Since the range of the  $s$  is always between  $-0.3$  and  $0.3$ , equation (6) claims that under normal operation, the rotor EMF operates with a low amplitude.

Under the fault, the rotor EMF in the rotor frame can be expressed as:

$$\vec{e}_r^r = \frac{L_m}{L_s} \frac{d\vec{\psi}_s^r}{dt} = \frac{2(1-p)V_{L1}}{\pi} \frac{L_m}{L_s} \left[ s e^{j\omega_{slip} t} + \sum_{n=1}^{\infty} \frac{6n \pm s}{(6n \pm 1)^2} e^{\pm j(6n\pm 1)\omega_s t} e^{-j\omega_r t} \right] + \frac{2pV_{L1}}{\pi} \frac{L_m}{L_s} \left[ (1-s) + \sum_{n=1}^{\infty} \frac{\pm(1-s)}{(6n \pm 1)^2} e^{-j\omega_r t} e^{-\frac{t}{\tau_s}} \right] \quad (7)$$

where  $\tau_s$  represents the stator time constant. From equation (7), the existence of the second term makes the amplitude of the rotor EMF several times larger than that of the normal operation. Therefore, hardware-based DC voltage restoration is necessary for the DC-DFIG to protect the fragile rectifier and converter.

### 3.2. IDC

Internet data centers (IDCs) primarily contain analog and digital devices used for data processing (servers), data storage (storage equipment), and communications (network equipment) [60]. The global progress of internet-based technologies such as Cloud Computing, Big Data, and Artificial Intelligence are increasingly relying on the uninterrupted operation of data centers in order to successfully achieve their day-to-day objectives.

With the control of power electronic converters, IDC is always modeled as a CPL. The CPL is nonlinear and exhibit a negative impedance voltage-current characteristic [61,62]. Therefore, when an abrupt.

Voltage sag or swell occurs, there will be a huge transient overcurrent inside the IDC. Meanwhile, if the amplitude or duration time of the voltage sag/swell exceeds the voltage tolerant curves defined either by the Computer Business Equipment Manufacturers Association (CBEMA), or the Information Technology Industry Council (ITIC) [63], the servers inside the IDC are under the risk of interruption, resulting in data loss, cooling problems, and huge economic loss.

### 3.3. SCI-SMES

The structure of the proposed SCI-SMES is shown in Fig. 6. It mainly consists of two converters (Converter 1 and 2), an SMES coil, and two capacitors. The adopted converter is made up of four bridge arms, and each arm has a controllable switch and a diode connected in serial. The switch group  $[S_2 \sim S_4]$  have an inversely ON-OFF state with the group  $[S_1 \sim S_3]$ , and so do the switch groups  $[Q_2 \sim Q_4]$  and  $[Q_1 \sim Q_3]$ . The SMES coil is connected between the joints  $C_1$  and  $D_2$ . Joints  $A_1$  and  $A_2$  connect in series with the two different loads #1 and #2, whereas joints  $B_1$  and  $B_2$  are linked with the two different DC grids. Obviously, the relationship among  $v_{g1}$  and  $v_{g2}$ ,  $v_{L1}$  and  $v_{L2}$ , and  $v_{c1}$  and  $v_{c2}$  can be expressed as:

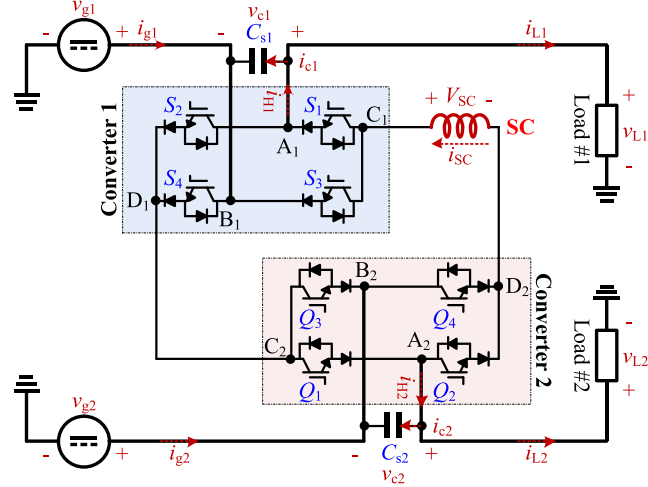


Fig. 6. Structure of the SCI-SMES.

$$\begin{cases} v_{g1} = v_{L1} + v_{c1} \\ v_{g2} = v_{L2} + v_{c2} \end{cases} \quad (8)$$

There are four statuses depending on the switching operations of the Converter 1 and 2, as shown in Fig. 7. According to the relationship between the SMES current  $i_{SC}$  and the load currents  $i_{L1}$  and  $i_{L2}$ , the duty cycles  $D_1$  and  $D_2$  of the converters 1 and 2 can be expressed as:

$$\begin{cases} D_1 = \frac{1}{2} \left( 1 - \frac{i_{L1}}{i_{SC}} \right) \\ D_2 = \frac{1}{2} \left( 1 - \frac{i_{L2}}{i_{SC}} \right) \end{cases} \quad (9)$$

As depicted in (9), when  $i_{L1} > i_{L2}$ , there is  $D_1 < D_2$  and the status sequence of the circuit in one period is: (a)→(d)→(c). Conversely, when  $i_{L1} > i_{L2}$ , the status sequence of the circuit in one period should be: (a)→(b)→(c). According to the above analysis, the duty cycle  $D_1$  and  $D_2$  are both in the range of  $(0, 0.5)$ .

The stable value of the  $i_{SC}$  can be approximately estimated following Ref. [42] as:

$$i_{SC} \approx \sqrt{\frac{(v_{c1} i_{L1} + v_{c2} i_{L2})}{2R_{SC}}} \quad (10)$$

Equation (10) reveals that the stored current  $i_{SC}$  depends on the leakage resistance of the SMES, the voltage difference ( $v_{c1}$  and  $v_{c2}$ ), and the current of load #1 and #2 ( $i_{L1}$  and  $i_{L2}$ ), and have no concern with the SMES inductance  $L_{SC}$ . Therefore, a more considerable SMES inductance can bring a bigger capacity for voltage compensation.

The control system is shown in Fig. 8. The measured two load voltages are used as the input signals. The differences between the reference and actual signals are regulated via two proportional-integral plus resonance (PI-R) controllers. The output duty cycle  $D_1$  and  $D_2$  can be generated from the PI-R controllers, adding the offset constant of 0.5. The control signals of  $S_1 \sim S_4$  and  $Q_1 \sim Q_4$  can be obtained by comparing the duty cycle  $D_1$  and  $D_2$  with the triangular carrier.

Second-order voltage ripples of the DC microgrids are also common power quality issues, mainly resulting from the voltage unbalance of the AC grid, as reported in Ref. [27]. Therefore, in the control system of the SCI-SMES, a resonance (R) controller with second-order frequency is added to implement the voltage ripple mitigation.

### 4. Experiment of SCI-SMES

A kW-class 10-mH/120-A SMES-based test system is established with

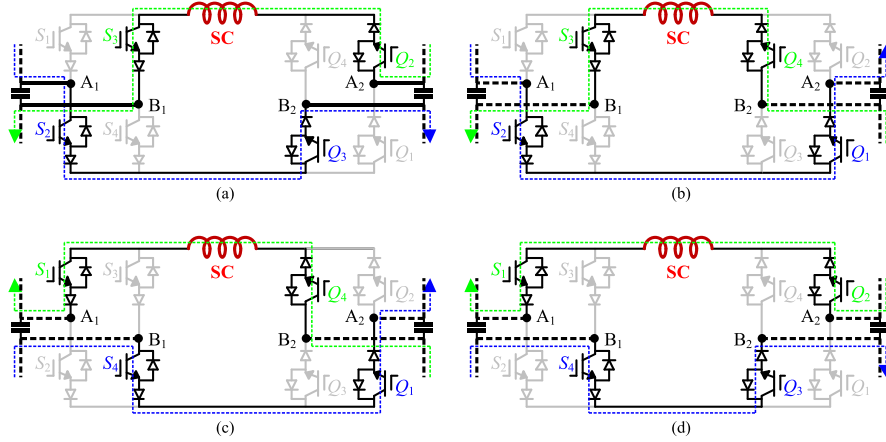


**Fig. 7.** Four statuses of the SCI-SMES under operation.

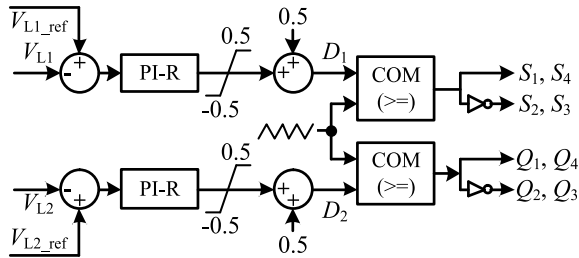


**Fig. 8.** Control strategies of the two converters.

consideration of a 24-V/24-A and a 48-V/12-A DC system, respectively. The experimental setup is shown in Fig. 9. The adopted SMES is with a varying-axial-gap structure, and detailed design about this new kind of SMES coil has been reported in Ref. [64]. In the small-scale experiments, the tested SMES magnet prototype is basically a solenoid formed by six series-connected double pancakes. The axial gaps between adjacent assemblies from one end to the other end are 20 mm, 18 mm, 16 mm, 18 mm, 20 mm, as shown in Fig. 10(a). The height, inner and outer radius of each pancake are 9.6 mm, 100 mm and 109.6 mm [65]. This SMES magnet prototype in Fig. 10(b) has an inductance of 10.1 mH and a critical current of 123.8 A. With the uneven axial gaps between adjacent pancakes, the critical current is increased from the original 102.3 A to an optimized value of 123.8 A. The SMES coil and sixteen power electronic

devices in the two converters are fully immersed in liquid nitrogen at 77 K to achieve a new cryogenic power conversion system for the SCI-SMES. Compared to the room-temperature power conversion system, this new cryogenic SMES converter can improve the overall energy efficiency and eliminate the overheating risk of power electronics [66, 67].

Fig. 11 shows the responses of the grid side voltages, load voltages ( $v_{g1}$ ,  $v_{g2}$ ,  $v_{L1}$ , and  $v_{L2}$ ), load currents ( $i_{L1}$  and  $i_{L2}$ ), and SMES current ( $i_{SC}$ ) under four voltage sag and swell cases:

**Case 1.** voltage swell in load #1 and load #2.

**Case 2.** voltage sag in load #1 and voltage swell in load #2.

**Case 3.** voltage swell in load #1 and voltage sag in load #2.

**Case 4.** voltage sag in load #1 and load #2.

Under four cases, the voltage can be well-maintained at the rated values (24-V and 48-V), respectively. As can be seen, the current stored in the SMES can be kept at ~52 A under normal operation. When the voltage sag or swell occurs, the SMES current will be reduced or increased to compensate the lacking load energy or absorb the surplus load energy, respectively. After the fault clearance, the SMES current will be automatically recovered to ~52 A. The voltage sag and swell experiments validate the effectiveness of the proposed SCI-SMES.

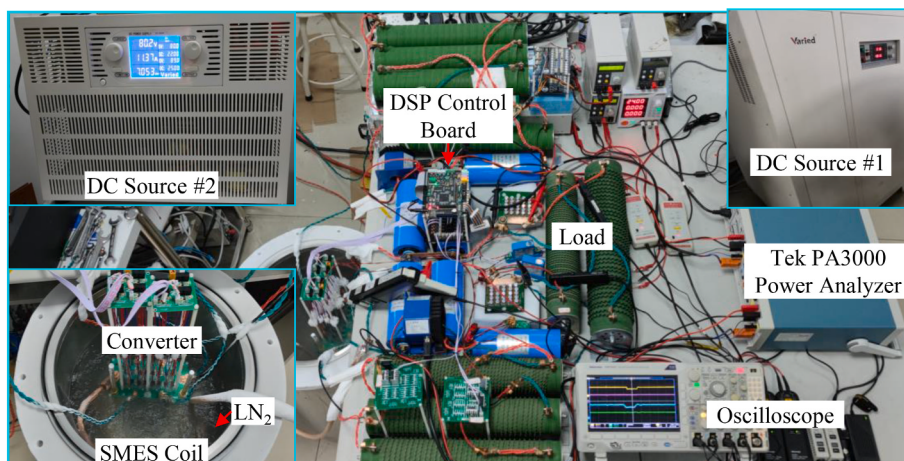


**Fig. 9.** Experimental platform for the SCI-SMES.

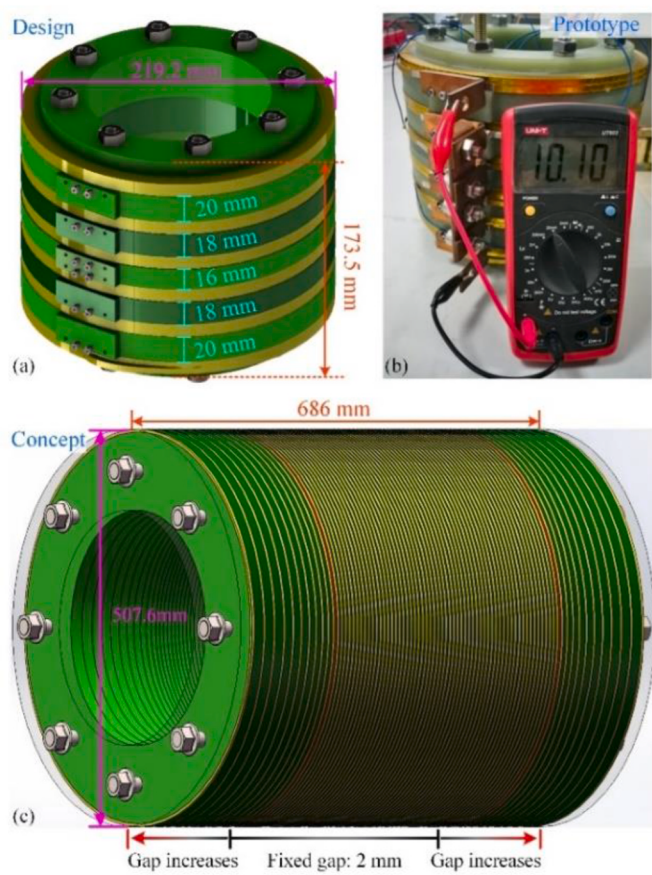


**Fig. 10.** Experimental and conceptual magnets. (a) Structural design of the 10-mH/120-A SMES. (b) Prototype of the 10-mH/120-A SMES. (c) Structural design of the 2.57-H/900-A SMES.

## 5. Case study

### 5.1. Model configuration

In order to verify the performance of the proposed hybrid MV DC power system, the model with the integrations of the DFIG-DC system, IDC, SCI-SMES.

And DCPET 1 and 2 has been built up in Matlab/Simulink. The whole structure of the system is shown in Fig. 1. The DC-DFIG and the IDC are both considered as 1 MW. The rated voltage of the MV DC bus is 10 kV, and the transformer ratios of the DCPET 1 and 2 are 10 kV/3 kV and 10 kV/1.5 kV, respectively. The rated transmission-line currents of the DC-DFIG and the IDC are 330 A and 670 A, respectively.

### 5.2. Design of the SMES magnets

The successful design and practical winding of the SMES magnet prototype mentioned in the scaled-down experiment lay a firm base for designing a high-capacity SMES magnet used in the following high-power hybrid MV DC power system. Fig. 10(c) shows the structural evolution from conventional solenoidal magnet structure with all-same constant axial gaps among pancakes, to a new structure with varying axial gaps among certain end pancakes. After the structural optimization of a MJ-class SMES magnet, the critical current and energy capacity improve by 20.46% and 38.67%, respectively. The inductance, critical current and energy storage capacity of the optimized SMES magnet are 2.57 H, 900 A and 1 MJ, respectively. To meet the demand from the interline energy conversion and management in the hybrid MV DC power system, eight 1-MJ SMES units are adopted to form a 5.14-H/

1800-A assembly by using series-parallel combination.

### 5.3. Short-term power imbalance with the protection of SCI-SMES

To directly analysis the voltage compensation performance of the SCI-SMES, possible scenarios of the voltage disturbances in the hybrid MV DC power system are listed as follows:

- 1) When the RCB is OFF and a symmetrical voltage sag or swell occurs in the AC grid 1, the DC-DFIG-side MV DC bus will experience a DC voltage sag or swell;
- 2) When the RCB is OFF and a symmetrical voltage sag or swell occurs in the AC grid 2, the IDC-side MV DC bus will experience a DC voltage sag or swell;
- 3) When the RCB is ON and a symmetrical voltage sag or swell occurs in the AC grid 1 or 2, both the DC-DFIG and the IDC will experience a DC voltage sag or swell;
- 4) When the RCB is ON and an asymmetrical voltage fault occurs in the AC grid 1 or 2, both the DC-DFIG and the IDC will experience a DC oscillation.

Therefore, several voltage disturbances have been set in the simulation. The sag/swell amplitude and the time duration are with the consideration of the grid code (U.S. PREPA).

- 1) During  $t = 10.5 \text{ s} - 11.125 \text{ s}$ , an 85% depth of DC voltage sag occurs at the DC-DFIG-side MV DC bus;
- 2) During  $t = 11.625 \text{ s} - 12.625 \text{ s}$ , a 40% height of DC voltage swell occurs at the DC-DFIG-side MV DC bus;
- 3) During  $t = 13.125 \text{ s} - 13.75 \text{ s}$ , an 85% depth of DC voltage sag occurs at the IDC-side MV DC bus;
- 4) During  $t = 14.25 \text{ s} - 15.25 \text{ s}$ , a 40% height of DC voltage swell occurs at the IDC-side MV DC bus;
- 5) During  $t = 15.75 \text{ s} - 16.375 \text{ s}$ , an 85% depth of DC voltage sag occurs at both the DC-DFIG- and the IDC-side MV DC bus;
- 6) During  $t = 16.875 \text{ s} - 17.875 \text{ s}$ , a 40% height of DC voltage swell occurs at both the DC-DFIG- and the IDC-side MV DC bus.

The above fault configuration is shown in Fig. 12(a). Since the time durations of the power quality disturbances are always short, the wind speed of the DC-DFIG and the power demand of the IDC are assumed constant to simplify the analysis.

Fig. 12(b) and (c) show the terminal voltage and current responses of the DC-DFIG and IDC without SCI-SMES. As can be seen, there are huge voltage and current spikes at each time of the fault occurrence and clearance. Table 1 shows the values of these spikes. Most of them are beyond the maximum permitted values of the voltage (0.9 pu and 1.1 pu) and current (2.0 pu). Under voltage oscillation sag, the total harmonic distortions (THDs) of the IDC and the DC-DFIG are both beyond 5%.

From Fig. 12(d), (e) and Table 2, it can be seen that with the protection of the SCI-SMES, all the spikes of voltage disturbances can be limited within 0.9 pu and 1.1 pu. The over-currents can be well-constrained within 1.2 pu. With the oscillation control of the SCI-SMES, the THDs of the currents are reduced within 5%, guaranteeing the stability of the DC-DFIG and IDC under FRT operation.

Fig. 12(f) shows the responses of the energy exchanges among SMES and transmission lines of DC-DFIG and IDC. The simulation results are consistent with the theoretical analysis in Section 2.5. In the DC-DFIG part, when a voltage sag occurs, the SMES absorbs the surplus power generation from the DC-DFIG, and the variation of the SMES stored energy ( $\Delta E_{\text{SMES}}$ ). Conversely, when a voltage swell occurs, the  $\Delta E_{\text{SMES}}$  decrease. The energy conversion between the SMES and IDC part has a complementary process with that of the DC-DFIG part. Under both voltage sag condition, as shown in Fig. 12(f), the energy transformation direction is: DC-DFIG → SMES → IDC. Whereas, under both voltage swell

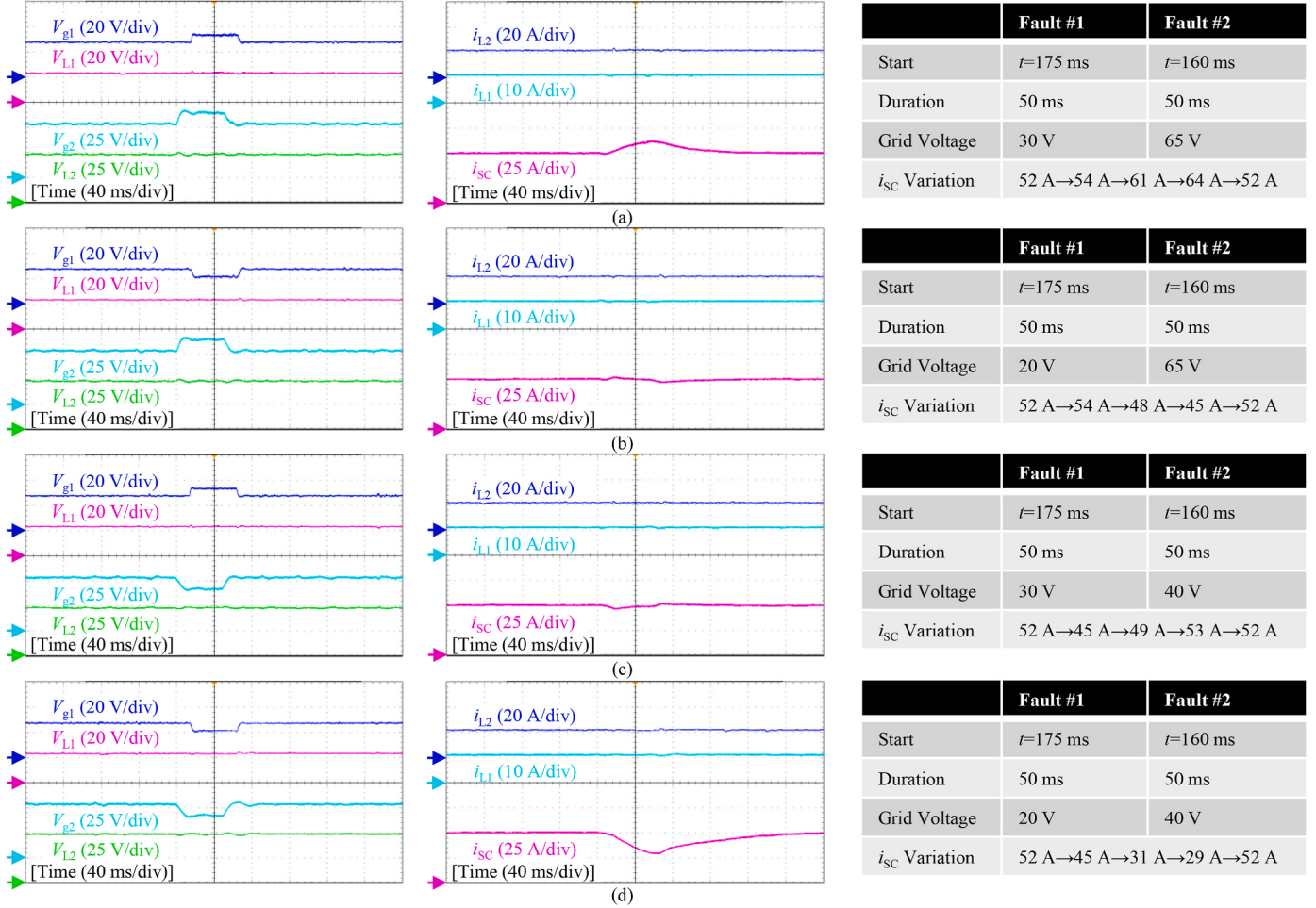


Fig. 11. Voltage compensation effect with SCI-SMES: (a) under Case 1; (b) under Case 2; (c) under Case 3; (d) under Case 4.

conditions, the power transformation direction is: DCPET2  $\rightarrow$  SMES  $\rightarrow$  DCPET1. Since the IDC and the DC-DFIG has the same power level, the SMES has almost no current variation. Therefore, the design of the SMES capacity can be significantly reduced.

## 6. Economic evaluation

### 6.1. Cost evaluation of SCI-SMES

The economic evaluation of the proposed SCI-SMES ( $C_{SCI-SMES}$ ) refers mainly to the investment cost and operating & maintenance (O&M) cost. The investment cost consists of the SMES cost ( $C_{SMES}$ ), cryogenic cost ( $C_{cold}$ ) and converter cost ( $C_{Converter}$ ), i.e.:

$$C_{SCI-SMES} = \underbrace{(C_{SMES} + C_{cold} + C_{Converter})}_{C_{investment}} + NC_{O\&M} \quad (11)$$

- 1) SMES cost: the adopted SMES in simulation forms of eight 2.57-H/900-A SMES units. The total length of the superconducting tape of each SMES unit is 5 km [64]. Considering the cost of the superconducting tape (28.24 k€/km), the energy capital cost of the SMES system is 1129.46 k€.
- 2) Cryogenic cost: the heat power of the SMES system is mainly resulted from the current leads. The typical value of the heat load is around 50 W/kA from 300 K to 77 K and 0.5 W/kA from 77 K to 20 K [68]. Since each SMES unit has two current leads with the current 900 A, its heat power can be calculated as 90 W, and the heat power of the whole SMES system can be determined to be 720 W. The 20-K

refrigerator cost can be obtained from the following experience equation [69]:

$$C_{cold}(k\text{€}) = 8.87R(W)^{0.412} \quad (12)$$

From (12), the cryogenic cost can be calculated as 133.34 k€.

- 3) Converter cost: the converter cost is one of the main costs of the SCI-SMES. According to Ref. [70], the unit cost of the converter is 360.27 €/kW. Considering the SCI-SMES has two ports and the rated power of each port is 1.5 MW, the total cost of the converter is 1080.81 k€.
- 4) O&M cost: the total O&M cost includes three parts: SMES cost, cryogenic cost and converter cost. According to Ref. [71], the SMES O&M cost is about 17.66 €/kW/year. Thus, the annual O&M cost of the 3-MW SMES can be estimated to be 52.98 k€/year. The cryogenic O&M cost consists of two parts. The first part is the electricity cost for the operation of the refrigerator. According to Ref. [69], the refrigerating efficiency of the chiller at 20 K is 14.5%, then it consumes 43.50 MWh of electricity every year. Considering a typical unit cost of 0.1€/kWh, the annual electricity cost is 4.35 k€. The second part is the maintenance cost of the refrigerator. Considering a typical maintenance cost proportion of 5%, the annual maintenance cost of the refrigerator is about 6.67 k€. The O&M cost of the converter is about 9.54 €/kW/year. The total O&M cost of the 3-MW SCI-SMES can be estimated as 92.62 k€/year. The SCI-SMES cost for investment and O&M is show in Fig. 13.

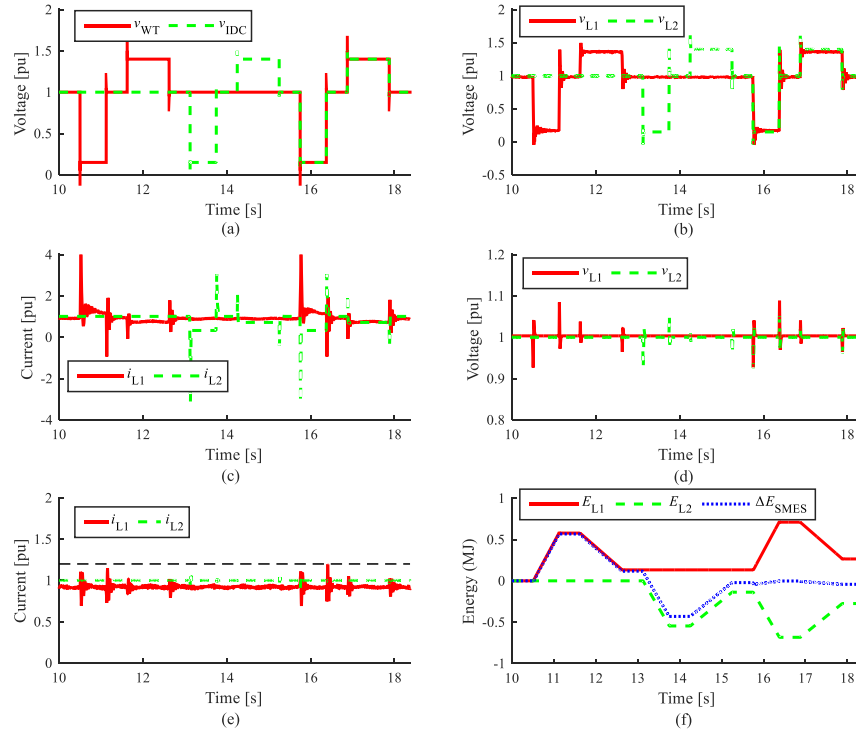


**Fig. 12.** (a) Grid-side voltage of WT line and IDC line. (b) Terminal voltage of WT and IDC without protection. (c) Terminal current of WT and IDC without protection. (d) Terminal voltage of WT and IDC with SCI-SMES. (e) Terminal current of WT and IDC with SCI-SMES. (f) Energy conversion of WT, IDC, and SMES.

**Table 1**  
Parameters of WT and IDC without protection.

Parameter	WT Sag	WT Swell	IDC Sag	IDC Swell	Both Sag	Both Swell	Oscillation
WT current	<b>4.09 pu</b>	1.79 pu	–	–	<b>4.01 pu</b>	1.81 pu	1.44 pu
WT voltage	–0.05 pu	<b>1.49 pu</b>	–	–	–0.04 pu	<b>1.50 pu</b>	<b>0.66 pu</b>
WT EM torque	<b>–2.36 pu</b>	–2.11 pu	–	–	–2.35 pu	–2.13 pu	1.46 pu
WT rotor current	<b>2.72 pu</b>	1.56 pu	–	–	<b>2.58 pu</b>	1.62 pu	1.34 pu
IDC current	–	–	<b>3.15 pu</b>	<b>2.09 pu</b>	<b>3.15 pu</b>	<b>2.09 pu</b>	1.80 pu
IDC voltage	–	–	–0.03 pu	<b>1.65 pu</b>	–0.03 pu	<b>1.65 pu</b>	0.60 pu
WT current (THD)	–	–	–	–	–	–	<b>5.80%</b>
IDC current (THD)	–	–	–	–	–	–	<b>14.41%</b>

**Table 2**  
Parameters of WT and IDC with SCI-SMES.

Parameter	WT Sag	WT Swell	IDC Sag	IDC Swell	Both Sag	Both Swell	Oscillation
WT current	1.15 pu	1.02 pu	–	–	1.19 pu	1.02 pu	0.96 pu
WT voltage	0.93 pu	1.04 pu	–	–	0.93 pu	1.04 pu	0.98 pu
WT EM torque	–1.34 pu	–1.22 pu	–	–	1.37 pu	1.23 pu	1.17 pu
WT rotor current	1.27 pu	1.19 pu	–	–	1.25 pu	1.23 pu	1.17 pu
IDC current	–	–	1.05 pu	1.04 pu	1.05 pu	1.04 pu	1.02 pu
IDC voltage	–	–	0.93 pu	1.02 pu	0.92 pu	1.05 pu	0.98 pu
WT current (THD)	–	–	–	–	–	–	2.39%
IDC current (THD)	–	–	–	–	–	–	3.95%

## 6.2. Economic loss analysis of DC-DFIG and IDC

Ref. [72] has considered a typical industry based standard method used for characterizing voltage sag by minimum voltage sag magnitude. The economic loss relation with severity can be shown by a matrix of weighting factor ( $k_w$ ). Residual voltages below 40%, between 40% and 70%, and above 70% can be equivalent to 80%, 40% and 10% of the economic loss causes by a momentary interruption, respectively. Referring to the 2021 data center industry survey results report released by Uptime Institute, a data center downtime will cost 96 k€ in economic

losses ( $L_{IDC}$ ) [73]. According to the practical grid voltage sag frequency ( $T_{sag}$ ) provided by Ref. [74], the economic loss caused by the voltage sag of the data center can be expressed as:

$$C_{IDC} = \sum k_{IDC} T_{sag} L_{IDC} \quad (13)$$

The calculated data from (13) is shown in Table 3.

The economic loss of the DC-DFIG mainly depends on the converter cost. According to Ref. [74], the capital cost of the wind-turbine-utilized converter is around 360.27 €/kW. Note that the capacity of the converter in DC-DFIG is only 30% of the rated power, the converter can be

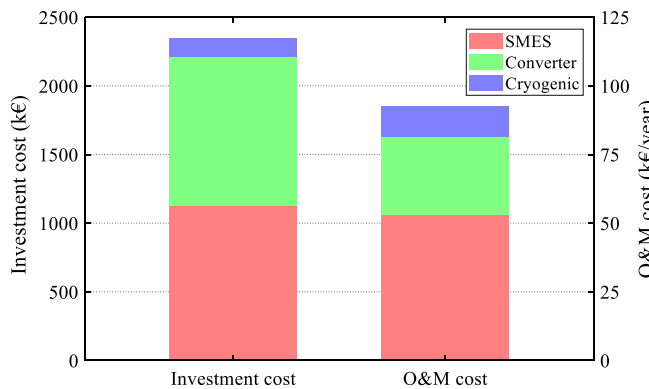


**Fig. 13.** The SCI-SMES cost for investment, and operating & maintenance (O&M).

**Table 3**  
IDC economic loss analysis caused by voltage sags.

Residual voltage	Weighting factor ( $k_{IDC}$ )	Events per year ( $T_{sag}$ )	Equivalent interruptions	Economic loss(k€)
0.1–0.2	0.8	0.8476	0.67808	65.09
0.2–0.3	0.8	1.4025	1.122	107.71
0.3–0.4	0.8	2.0171	1.61368	154.91
0.4–0.5	0.4	2.7726	1.10904	106.47
0.5–0.6	0.4	3.593	1.4372	137.97
0.6–0.7	0.4	4.6109	1.84436	177.06
0.7–0.8	0.1	5.9419	0.59419	57.04
0.8–0.9	0.1	6.9578	0.69578	66.79
Total ( $C_{IDC}$ )	–	–	9.09433	873.04

estimated at 162.13 k€ ( $L_{WT}$ ). Fig. 14(a) shows the DC current under 20%, 34% and 50% voltage sag ratios ( $p$ ). Fig. 14(b) shows the relationship between the DC fault current and the voltage sag ratio. Considering the maximum withstand current of the converter is twice

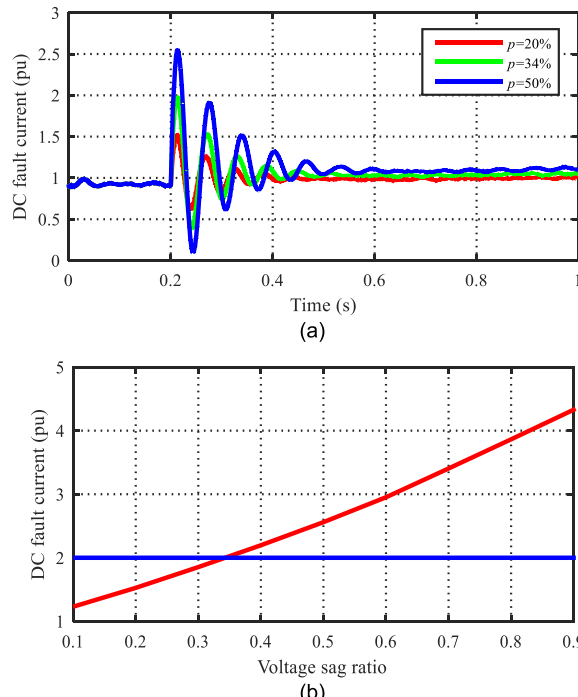


**Fig. 14.** (a) DC current response under 20%, 34%, and 50% voltage sag ratio.  
(b) Relationship between voltage sag ratio and DC fault current.

the rated current, the converter will be destroyed when the voltage sag ratio exceeds 0.34 according to Fig. 13. From the voltage sag frequency data in Table 3, the economic loss ( $C_{WT}$ ) of the DC-DFIG can be expressed as:

$$C_{WT} = \sum k_{WT} T_{sag} L_{WT} \quad (14)$$

The weighting factor of the economic loss of DC-DFIG and other critical parameters are shown in Table 4.

### 6.3. Static payback period analysis

From the capital cost of the SCI-SMES and the economic loss data in Tables 3 and 4, the static payback period ( $N_p$ ) of the whole SCI-SMES system can be calculated:

$$N_p = \frac{C_{Investment}}{\delta(C_{IDC} + C_{WT}) - C_{O\&M}} \quad (15)$$

Considering the possibility that the sensitive devices in IDC and DC-DFIG can successfully ride through the voltage sag, a damage ratio  $\delta$  is introduced. When the  $\delta$  is considered at 10%, 15%, and 20%, respectively, the relationship between the  $C_{SCI-SMES}$  and  $C_{IDC} + C_{WT}$  is drawn in Fig. 15. It can be seen that the cost-recovering times of the SCI-SMES is 11.06, 6.44, and 4.54 years, respectively.

### 6.4. Dynamic payback period analysis

In order to evaluate the dynamic payback period of the proposed SCI-SMES scheme in a more realistic way, the annual real discount rate  $i_{dis}$  derived from the nominal discount rate and the expected inflation rate can be used [75]:

$$i_{dis} = \frac{i' - f}{1 + f} \quad (16)$$

where  $i'$  is the nominal discount rate (8%) and  $f$  is the expected inflation rate (2%).

The present worth factor (PWF) is to convert a future value to a present value [76]:

$$PWF = \frac{1}{(1 + i_{dis})^y} \quad (17)$$

where the index  $y$  is the year in the range of the overall device lifetime. Therefore, the net annual income (NAI) for the SCI-SMES can be calculated by:

$$NAI_y = \frac{\delta(C_{IDC} + C_{WT}) - C_{O\&M}}{(1 + i_{dis})^y} \quad (18)$$

The NAI in this work indicates an equivalent cash income obtained by saving the economic loss during uncertain voltage sags.

The discounted payback period (DPP) is the dynamic period (calculated as years) needed to earn back the initial investment through the cash inflow to avoid the economic losses of IDC and DC-DFIG

**Table 4**  
Economic loss analysis of DC-DFIG.

Residual voltage	Weighting factor ( $k_{WT}$ )	Events per year ( $T_{sag}$ )	Equivalent interruptions	Economic loss(k€)
0.1–0.2	1	0.8476	0.8476	136.45
0.2–0.3	1	1.4025	1.4025	227.39
0.3–0.4	1	2.0171	2.0171	327.03
0.4–0.5	1	2.7726	2.7726	449.52
0.5–0.6	1	3.593	3.593	582.53
0.6–0.7	0.6	4.6109	2.7665	448.54
0.7–0.8	0	5.9419	0	–
0.8–0.9	0	6.9578	0	–
Total ( $C_{WT}$ )	–	–	13.3993	2171.46

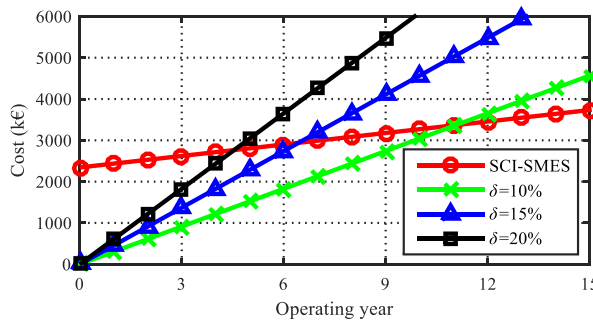


**Fig. 15.** Comparisons of the SCI-SMES cost and the economic losses of IDC and DC-DFIG considering long-term static operations.

(considering a money discount), which can be calculated:

$$\sum_{y=1}^{DPP} NAI_y - C_{\text{Investment}} = 0 \quad (19)$$

Fig. 16 shows the payback period comparisons between the static and dynamic analyses. The payback periods increase if we consider the discount rate during actual operations. For the fixed 3 MW SCI-SMES system, the payback period goes up from 11.06 to 18.41 years with a device damage ratio of 0.1. Moreover, with a decreasing damage ratio for the IDC and DC-DFIG applications, the differences between static and dynamic payback periods will be smaller. For example, when the damage ratio reaches 0.2, the static and dynamic payback periods are 4.54 and 5.44 years (only 1.2 times difference). Therefore, for the practical design, the proposed SCI-SMES scheme is favorable for the occasions having relatively high device damage ratios during grid faults. On this basis, the payback period of the investment will also decline, which is able to enhance both the working performance and economic benefits of the SCI-SMES scheme, to achieve the technical-economic superiority.

## 7. Conclusion

In this paper, an advanced concept of DC-DFIG/IDC hybrid MV DC network has been investigated for the multi-line power quality enhancement and the interline energy management by integrating a SCI-SMES power device. The proposed SCI-SMES is able to implement both short-term power flow and long-term energy interaction operations among multiple DC power lines in the DC-DFIG/IDC hybrid MV DC network. With the energy conversion and management of the SCI-SMES and DCPETs, the conceptual design of the multi-energy hybrid DC system guarantees the energy consumption of the renewable energy and the dual power supply insurance of the sensitive load under voltage faults. It not only fits the FRT requirement of the future DC power system, but also provides a novel reference to the renewable/sensitive-load integrated DC power systems. An experimental prototype has been developed and tested for verifying the feasibility of the system simulation, which can further clarify the superiority in actual renewable and sustainable energy scenarios. Economic analysis of the SCI-SMES, IDC, and DC-DFIG proves the feasibilities of the proposed SCI-SMES in practical applications.

Conclusively, the overall characteristics and technical advantages of the SCI-SMES are concluded as follows:

- *Concise Topology and Straightforward Control:* unlike existing dual-active-bridge-based voltage regulators with complicated transformer and multi-converter, the proposed topology only contains eight controllable power-electronic switches and a SMES unit. The control system is also implementable in practice.
- *Non-Interacting Voltage Compensation:* experiments and simulations show that if one converter is faulty during the voltage compensation

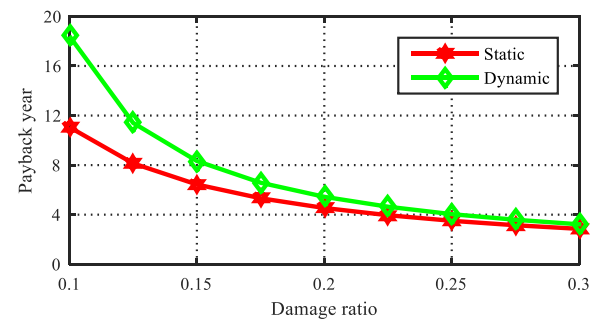


**Fig. 16.** Comparisons of the static and dynamic payback periods: 3-MW SCI-SMES system in the DC-DFIG/IDC hybrid network.

process, the compensation capability of the other converter is not influenced.

- *Self-Charging and Economic Consideration:* after fault clearance, the SMES current can automatically recover to the normal value. Experiments prove the current self-recovery ability of the proposed SCI-SMES. Meanwhile, the interline structure improves the energy utilization rate, and the overall cost of the SMES-based device can be greatly reduced for a multi-line microgrid.

The existing SCI-SMES solution still has following shortcomings which can be further improved: (1) the energy capital cost of the SMES is still high to compensate long-time voltage fluctuations; (2) according to equation (10), the SMES operating current will be in a high level when the SCI-SMES serves for high-power generators/loads, and the large operating current may bring high operating losses and extra risks.

To overcome the above-mentioned shortcomings, shorten the payback period, and further expand the application areas, the following efforts can be done in the future: 1) in order to reduce the capital cost, emerging technologies such as cost-effective SMES/battery hybrid energy storage can be utilized, which is equipped with fast response and large energy capacity; 2) voltage boosters, including DC power electronic transformers and DC/DC boost converters, can be used to increase the operating voltage level of the SMES, and can thereby reduce the operating current to cut down power losses and corresponding costs.

## Credit author statement

Conceptualization: Xiaoyuan Chen. Investigation: Ruohuan Yang, Mingshun Zhang, Boyang Shen. Methodology: Xiaoyuan Chen, Ruohuan Yang. Software: Ruohuan Yang, Shan Jiang, Huayu Gou. Visualization: Mingshun Zhang, Shan Jiang, Zhou Pang. Writing-Original draft: Xiaoyuan Chen, Ruohuan Yang. Writing-Reviewing and Editing: Ruohuan Yang, Boyang Shen. Supervision: Ruohuan Yang, Boyang Shen, Xiaoyuan Chen.

## Declaration of competing interest

The authors declare that they have no known competing financial interests or personal relationships that could have appeared to influence the work reported in this paper.

## Data availability

Data will be made available on request.

## Acknowledgements

This work was supported in part by the National Natural Science Foundation of China under Grant No. 51807128, Sichuan Science and Technology Program under Grant 2022YFG0304.

## References

- [1] Hrncic B, Pfeifer A, Juric F, Duic N, Ivanovic V, Vusanovic I. Different investment dynamics in energy transition towards a 100% renewable energy system. *Energy* 2021;237:121526.
- [2] Chen XY, Jiang S, Chen Y, Lei Y, Zhang DH, Zhang MS, Gou HY, Shen BY. A 10 MW class data center with ultra-dense high-efficiency energy distribution: design and economic evaluation of superconducting DC busbar networks. *Energy* 2022;250:12382.
- [3] Miranda RF, Salgado-Herrera NM, Rodríguez-Hernández O, Rodríguez-Rodríguez JR, Robles M, Ruiz-Robles D. Distributed generation in low-voltage DC systems by wind energy in the Baja California Peninsula, Mexico. *Energy* 2022;242:122530.
- [4] Kumar JS, Raja SC, Nesamalar JJD, Venkatesh P. Optimizing renewable based generations in AC/DC microgrid system using hybrid Nelder-Mead - cuckoo Search algorithm. *Energy* 2018;158:204–15.
- [5] Li JW, Gee AM, Zhang M, Yuan WJ. Analysis of battery lifetime extension in a SMES-battery hybrid energy storage system using a novel battery lifetime model. *Energy* 2015;86:175–85.
- [6] Pinturat W, Hredzak B. Fully decentralized control strategy for heterogeneous energy storage systems distributed in islanded DC datacentre microgrid. *Energy* 2021;231:120914.
- [7] Zehra SS, Rahman AU, Ahmad I. Fuzzy-barrier sliding mode control of electric-hydrogen hybrid energy storage system in DC microgrid: modelling, management and experimental investigation. *Energy* 2022;239:122260.
- [8] Shen L, Cheng QM, Cheng YM, Wei L, Wang YJ. Hierarchical control of DC microgrid for photovoltaic EV charging station based on flywheel and battery energy storage system. *Elec Power Syst Res* 2020;179:106079.
- [9] Ji HR, Chen SR, Yu H, Li P, Yan JY, et al. Robust operation for minimizing power consumption of data centers with flexible substation integration. *Energy* 2022;248:123599.
- [10] Lotfi H, Khodaei A. Hybrid AC/DC microgrid planning. *Energy* 2017;118:37–46.
- [11] Xia YH, Long T. Chopperless fault ride-through control for DC microgrids. *IEEE Trans Smart Grid* 2021;12(2):965–76.
- [12] Wang YZ, Li QQ, Li B, Wei TL, Zhu Z, Li WW, et al. A practical DC fault ride-through method for MMC based MVDC distribution systems. *IEEE Trans Power Deliv* 2021;36(4):2510–9.
- [13] Zohrabi N, Shi J, Abdelwahed S. An overview of design specifications and requirements for the MVDC shipboard power system. *Int J Electr Power Energy Syst* 2019;104:680–93.
- [14] Dragicevic T, Lu XN, Vasquez JC, Guerrero JM. DC microgrids-part II: a review of power architectures, applications, and standardization issues. *IEEE Trans Power Electron* 2016;31(5):3528–49.
- [15] Srivastava C, Tripathy M. DC microgrid protection issues and schemes: a critical review. *Renew Sustain Energy Rev* 2021;151:111546.
- [16] Al-Shetwi AQ, Hannan MA, Jern KP, Mansur M, Mahlia TMI. Grid-connected renewable energy sources: review of the recent integration requirements and control methods. *J Clean Prod* 2020;253:119831.
- [17] Mirhosseini M. Sensitivity analysis, adaptability improvement and control of grid-connected photovoltaic power plants under grid frequency variations. *Sol Energy* 2019;184:260–72.
- [18] Mirkhassani S, Ong HC, Chong W, Leong K. Advances and challenges in grid tied photovoltaic systems. *Renew Sustain Energy Rev* 2015;49:121–31.
- [19] Power quality in internet data centers. Palo Alto, CA, USA: Electr Power Res Inst; 2007.
- [20] Mohammadi J, Afsharnia S, Vaez-Zadeh S. Efficient fault-ride-through control strategy of DFIG-based wind turbines during the grid faults. *Energy Convers Manag* 2014;78:88–95.
- [21] Raghavendran CR, Roselyn JP, Sowmmiya U, Devaraj D. Effective power transfer and reduced-order generalized integrator sequence based fault ride through strategy in grid connected DFIG based WECS. *Int J Electr Power Energy Syst* 2021;130:106809.
- [22] Gao Y, Bazargan M, Xu L, Liang W. DC fault analysis of MMC based HVDC system for large offshore wind farm integration. *Proc 2nd IET Renew Power Gen Conf* 2013;623:1–4.
- [23] Wang RT, Feng W, Xue HJ, Gerber D, Li YT, Hao B, et al. Simulation and power quality analysis of a loose-coupled bipolar DC microgrid in an office building. *Appl Energy* 2021;303:117606.
- [24] Li B, He JW, Li Y, Wen W, Li BT. A novel current-commutation-based FCL for the flexible DC grid. *IEEE Trans Power Electron* 2020;35(1):591–606.
- [25] Xue SM, Liu BB, Wang SX, Chen X, Zhu XS, Lu JC. A modular hybrid DC circuit breaker with fault current self-adaptive control and protection coordination. *Int J Electr Power Energy Syst* 2022;134:107434.
- [26] Zhu D, Zou X, Deng L, Huang Q, Zhou S, Kang Y. Inductance-emulating control for DFIG-based wind turbine to ride-through grid faults. *IEEE Trans Power Electron* 2017;32(11):8514–25.
- [27] Nejabatkhan F, Li YW. Overview of power management strategies of hybrid AC/DC microgrid. *IEEE Trans Power Electron* 2015;30(12):7072–89.
- [28] Eghedarpour N, Farjah E. Power control and management in a hybrid AC/DC microgrid. *IEEE Trans Smart Grid* 2014;5(3):1494–505.
- [29] Salomonsson D, Soder L, Sannino A. An adaptive control system for a DC microgrid for data centers. *IEEE Trans Ind Appl* 2008;44(6):1910–7.
- [30] Wessels C, Gebhardt, Fuchs FW. Fault ride-through of a DFIG wind turbine using a dynamic voltage restorer during symmetrical and asymmetrical grid faults. *IEEE Trans Power Electron* 2011;26(3):807–15.
- [31] Babaei E, Kangarlu MF. Operation and control of dynamic voltage restorer using single-phase direct converter. *Energy Convers Manag* 2011;52(8–9):2965–72.
- [32] Guo WY, Xiao LY, Dai ST. Enhancing low-voltage ride-through capability and smoothing output power of DFIG with a superconducting fault-current limiter-magnetic energy storage system. *IEEE Trans Energy Convers* 2012;27(2):277–95.
- [33] Gee AM, Robinson F, Yuan WJ. A superconducting magnetic energy storage-emulator battery supported dynamic voltage restorer. *IEEE Trans Energy Convers* 2012;32(1):55–64.
- [34] Chen X, Yan LF, Zhou X, Sun HS. A novel DVR-ESS-embedded wind-energy conversion system. *IEEE Trans Sustain Energy* 2018;9(3):1265–74.
- [35] Gontijo GF, Tricarico TC, da Silva LF, Krejci D, Franca BW, Aredes M, et al. Modeling, control, and experimental verification of a DFIG with a series-grid-side converter with voltage sag, unbalance, and distortion compensation capabilities. *IEEE Trans Ind Appl* 2020;56(1):584–600.
- [36] Zheng ZX, Xiao XY, Chen XY, Huang CJ, Zhao LH, Li CS. Performance evaluation of a MW-class SMES-BES DVR system for mitigation of voltage quality disturbances. *IEEE Trans Ind Appl* 2018;54(4):3090–9.
- [37] Nielsen JG, Blaabjerg F. A detailed comparison of system topologies for dynamic voltage restorers. *IEEE Trans Ind Appl* 2005;41(5):1272–80.
- [38] Farhad-Kangarlu M, Babazadeh-Dizaji R. DC dynamic voltage restorer (DC-DVR): a new concept for voltage regulation in DC systems. Tehran, Iran: Proc 9th Annu Power Electron Drives Syst Technol Conf (PEDSTC); 2018. p. 122–7.
- [39] Vuyyuru U, Maiti S, Chakraborty C, Pal BC. A series voltage regulator for the radial DC microgrid. *IEEE Trans Sustain Energy* 2019;10(1):127–36.
- [40] Zhao B, Song Q, Liu W, Xiao Y. Next-generation multi-functional modular intelligent UPS system for smart grid. *IEEE Trans Ind Electron* 2013;60(9):3602–18.
- [41] Yang RH, Jin JX, Zhou Q, Mu S, Abu-Siada A. Superconducting magnetic energy storage based DC unified power quality conditioner with advanced dual control for DC-DFIG. *J Mod Power Syst Clean Energy* 2022;10(5):1385–400. <https://doi.org/10.35833/MPC.E.2021.000354>.
- [42] Chen XY, Zhang MS, Jiang S, Gou HY, Xie Q, Chen Y, et al. An SMES-based current-fed transformerless series voltage restorer for DC-load protection. *IEEE Trans Power Electron* 2021;36(9):9698–703.
- [43] Chen X, Xie Q, Bian X, Shen B. Energy-saving superconducting magnetic energy storage (SMES) based interline DC dynamic voltage restorer. *CSEE J Power Energy Syst* 2022;8(1):238–48.
- [44] Gyugyi L, Sen KK, Schauder CD. The interline power flow controller concept: a new approach to power flow management in transmission systems. *IEEE Trans Power Deliv* 1999;14(3):1115–23.
- [45] Elserougi A, Massoud AM, Abdel-Khalik AS, Ahmed S, Hossam-Eldin AA. An interline dynamic voltage restoring and displacement factor controlling device (IVDFC). *IEEE Trans Power Electron* 2014;29(6):2737–49.
- [46] Gkavanoudis SI, Demoulas CS. Fault ride-through capability of a DFIG in isolated grids employing DVR and supercapacitor energy storage. *Int J Electr Power Energy Syst* 2015;68:356–63.
- [47] Shen YW, Ke DP, Sun YZ, Kirschen DS, Qiao W, Deng XT. Advanced auxiliary control of an energy storage device for transient voltage support of a doubly fed induction generator. *IEEE Trans Sustain Energy* 2016;7(1):63–76.
- [48] Li JW, Yang QQ, Robinson F, Liang F, Zhang M, Yuan WJ. Design and test of a new droop control algorithm for a SMES/battery hybrid energy storage system. *Energy* 2017;118:1110–22.
- [49] Olabi AG, Onumaegebu C, Wilberforce T, Ramadan M, Abdelkareem MA, Al-Alami AH. Critical review of energy storage systems. *Energy* 2021;214:118987.
- [50] Chen XY, Jiang S, Chen Y, Zou ZC, Shen BY, Lei Y, et al. Energy-saving superconducting power delivery from renewable energy source to a 100-MW-class data center. *Appl Energy* 2022;310:118602.
- [51] Tomita M, Suzuki K, Fukumoto Y, Ishihara A, Kasaka T, Kobayashi Y. Energy-saving railway systems based on superconducting power transmission. *Energy* 2017;122:579–87.
- [52] Tan XG, Li QM, Wang H. Advances and trends of energy storage technology in microgrid. *Int J Electr Power Energy Syst* 2013;44(1):179–91.
- [53] Marques GD, Iaccetti MF. DFIG topologies for DC networks: a review on control and design features. *IEEE Trans Power Electron* 2019;34(2):1299–316.
- [54] Xiao Y, Fahimi B, Rotea MA, Li Y. Multiple reference frame-based torque ripple reduction in DFIG-DC system. *IEEE Trans Power Electron* 2020;35(5):4971–83.
- [55] Wu C, Cheng P, Ye Y, Blaabjerg F. A unified power control method for standalone and grid-connected DFIG-DC system. *IEEE Trans Power Electron* 2020;35(12):12663–7.
- [56] Soares EL, Jacobina CB, Melo VFMB, Rocha N, da Silva ERC. Dual converter connecting open-end doubly fed induction generator to a DC-microgrid. *IEEE Trans Ind Appl* 2021;57(5):5001–12.
- [57] Jahromi MG, Mirzaeva G, Mitchell SD, Gay D. Powering mobile mining machines: DC versus AC power. *IEEE Ind Appl Mag* 2016;22(5):63–72.
- [58] Zahedi B, Norum LE. Modeling and simulation of all-electric ships with low-voltage DC hybrid power systems. *IEEE Trans Power Electron* 2013;28(10):4525–37.
- [59] Abad G, Lopez J, Rodriguez M. Doubly fed induction machine: modeling and control for wind energy generation. Hoboken, NJ, USA: Wiley-IEEE Press; 2011.
- [60] Guo C, Luo F, Cai Z, Zhao YD. Integrated energy systems of data centers and smart grids: state-of-the-art and future opportunities. *Appl Energy* 2021;301:117474.
- [61] Jin CQ, Bai XL, Yang C, Mao W, Xu X. A review of power consumption models of servers in data centers. *Appl Energy* 2020;265:114806.
- [62] Koot M, Wijnhoven F. Usage impact on data center electricity needs: a system dynamic forecasting model. *Appl Energy* 2021;291:116798.
- [63] IEEE recommended practice for powering and grounding electronic equipment. IEEE Std May 2006. 1100–2005.

- [64] Chen X, Pang Z, Gou H, Xie Q, Zhao R, Shi Z, et al. Intelligent design of large-size HTS magnets for SMES and high-field applications: using a self-programmed GUI tool. *Supercond Sci Technol* 2021;34:095008.
- [65] Feng YJ, Chen XY, Chen Y, Li MY, Zeng L, Xie Q. Numerical calculation and experimental verification of inductance and critical current characteristics in a solenoidal SMES magnet. *IEEE Trans Appl Supercond* 2019;29(2):5700305.
- [66] Chen Y, Chen XY, Li T, Feng YJ, Liu Y, Huang Q, et al. Experimental investigations of state-of-the-art 650-V class power MOSFETs for cryogenic power conversion at 77K. *IEEE J Electron Devices Soc* 2018;6:8–18.
- [67] Gui HD, Zhang ZY, Chen RR, Ren R, Niu JH, Li HG, et al. Development of high-power high switching frequency cryogenically cooled inverter for aircraft applications. *IEEE Trans Power Electron* 2020;35(6):5670–82.
- [68] Morandi A. HTS dc transmission and distribution: concepts, applications and benefits. *Supercond Sci Technol* 2015;28:123001.
- [69] Zhou X, Tang YJ, Shi J, Zhang C, Gang K, Zhang LH, et al. Cost estimation models of MJ class HTS superconducting magnetic energy storage magnets. *IEEE Trans Appl Supercond* 2018;28(4):5701105.
- [70] Qiu T, Faraji J. Techno-economic optimization of a grid-connected hybrid energy system considering electric and thermal load prediction. *Energy Sci Eng* 2021;9(9): 1313–36.
- [71] Kebede AA, Kalogiannis T, Mierlo JV, Berecibar M. A comprehensive review of stationary energy storage devices for large scale renewable energy sources grid integration. *Renew Sustain Energy Rev* 2022;159:112213.
- [72] Sharma A, Rajpurohit BS, Singh SN. A review on economics of power quality: impact, assessment and mitigation. *Renew Sustain Energy Rev* 2018;88:363–72.
- [73] 2021 data center industry survey results. 2021. <https://uptimeinstitute.com/2021-data-center-industry-survey-results>.
- [74] Li SY, Wang Y, Hu WX, Xiao XY. Estimation method for voltage sag occurrence frequency based on calculation of protection operating time characteristics. *IEEE Trans Instrum Meas* 2022;71:9001814.
- [75] Chen QQ, Gu Y, Tang ZY, Wang DF, Wu Q. Optimal design and techno-economic assessment of low-carbon hydrogen supply pathways for a refueling station located in Shanghai. *Energy* 2021;237:121584.
- [76] Gjelaj M, Traholt C, Hashemi S, Andersen PB. Cost-benefit analysis of a novel DC fast-charging station with a local battery storage for EVs. In: 2017 52nd international universities power engineering conference. UPEC); 2017. p. 1–6.